JMEPEG (2019) 28:5533–5540
https://doi.org/10.1007/s11665-019-04275-w

1059-9495/$19.00

Effect of Process Parameters on the Mechanical Properties of Hastelloy X Alloy Fabricated by Selective Laser Melting

Xiaoqing Ni, Decheng Kong, Liang Zhang, Chaofang Dong, Jia Song, and Wenheng Wu

(Submitted December 17, 2018; in revised form April 28, 2019; published online August 20, 2019)

Mechanical properties of Hastelloy X alloys fabricated by selective laser melting were investigated and compared with the wrought counterpart. Nano-inclusions (Mo-rich carbides) distributed at the sub-grain boundaries in the selective laser-melted (SLMed) Hastelloy X alloy, whereas micron-scale precipitations existed in the wrought counterpart. The molten pool boundaries widely existed in the SLMed substrate, which acted as an initial site for crack and led to poor plasticity. However, the ultimate tensile strength values of the SLMed Hastelloy X alloys were around 910 MPa and much higher than the wrought counterpart (∼ 750 MPa), which was mainly ascribed to the high-density dislocations enriched at the sub-grain boundaries. Process parameter effects on the mechanical properties were also delineated in this work, and the volumetric energy density for the best mechanical properties of the SLMed Hastelloy X alloy was in the range from 140 to 170 J/mm^3.

Keywords Hastelloy X, mechanical property, selective laser melting, transmission electron microscopy

1. Introduction

Hastelloy X alloys have been widely used for components and structural materials in the current-generation nuclear power plants because of the excellent high-temperature creep strength, anti-corrosion property and sensitization resistance (Ref 1, 2). However, the actual structure of the component in service is usually complex and precise, thus makes the traditional casting process more time-consuming and expensive, especially when the temporary replacement parts are required. In this case, selective laser melting (SLM), a promising method for fabricating high-performance materials, exhibits significant advantages, such as less post-processing steps and controlling of the spatial distribution of the composition and microstructure (Ref 3-6).

Prior to the development of SLM technique, laser melt technology was widely used to optimize the surface microstructure and improve the corrosion performance of materials (Ref 7-9). Huge effects were paid over the past decades in the optimization of printing devices, including highly reliable laser, inexpensive high-performance computing hardware and software. Currently, SLM has highlighted its unique advantages in producing metallic materials in comparison with other fabrication techniques (Ref 10-12). SLM uses a high-density energy source to melt powders followed by rapid solidification into solid parts. So far, the effect of processing parameters such as laser power, scanning speed and hatch distance on the microstructure and defects during solidification of various selective laser-melted (SLMed) parts are widely reported (Ref 13-21) and the most relevant, being TiAl6V4, 316L, AlSi10Mg, CoCr and Inconel 718, can be reliably printed so far (Ref 22-24). The quality of printed parts is the most challenge to be resolved, and there may be multiple factors for this: (1) the rapid cooling rate in solidification during the SLM process results in the formation of non-equilibrium phases with a large range of compositions (Ref 25-29); (2) the molten pool boundary inside the parts, as well as the pores, cracks and rough surface condition, would result in a severe drop in plasticity and durability. The optimized process parameters can result in better mechanical properties (Ref 30, 31) and Suryawanshi et al. (Ref 32) demonstrated a significant increase in the yield strength of SLMed 316L by optimizing the scanning direction, which was attributed to the refinement of the microstructure during rapid solidification. Martin et al. (Ref 33) introduced the nanoparticles of nucleants during additive manufacturing for aluminum alloys, and a crack-free and fine-grained microstructure was achieved, resulting in material strengths comparable to that of wrought counterpart. Tomusa et al. (Ref 34) investigated the effect of minor alloying elements on the crack-formation characteristics of the SLMed Hastelloy X alloy and found that that low Si and C contents can help in avoiding crack formation, whereas cracking propensity was relatively independent of Mn concentration.

To the authors' best knowledge, there were no related studies about the process parameter effects, such as laser power and laser scanning speed, on the mechanical properties of the SLMed Hastelloy X, and considering that the Hastelloy X was served in harsh environments, it is highly significant to further investigate the mechanical property with different microstructures. In this research, Hastelloy X was fabricated by SLM with

Xiaoqing Ni, Liang Zhang, Jia Song, and **Wenheng Wu**, Shanghai Engineering Research Center of 3D Printing Materials, Shanghai Research Institute of Materials, Shanghai 200437, China; and **Decheng Kong** and **Chaofang Dong**, Corrosion and Protection Center, Key Laboratory for Corrosion and Protection (MOE), University of Science and Technology Beijing, Beijing 100083, China. Contact e-mails: 15201461811@163.com and liangustb@126.com.

various parameters, and the microstructures were investigated by electron back-scattered diffraction (EBSD) and transmission electron microscopy (TEM). The mechanical properties were investigated using tensile experiments, and the fracture morphology was observed via scanning electron microscopy (SEM).

2. Experimental Procedures

2.1 Sample Preparation

The size distribution of the argon gas-atomized powder and the morphology of the powder particles are shown in Fig. 1(a), and the average diameter was around 32 μm for Hastelloy X powders. The chemical compositions of the powders used for the SLMed components were similar with the traditional wrought Hastelloy X (wt.%): Fe 18.99, Cr 21.45, Mo 8.73, Mn 0.45, Si 0.45, C 0.075, P 0.006, N 0.02 and Ni balance, as given in Fig. 1(c). The laser scan way was designed according to a computer-generated path, and the printing process is repeated layer by layer by lowering the platform until the whole objects are totally fabricated.

Samples were manufactured using an EOS M290 system (Germany), which was equipped with a 400WYb/YAG fiber laser (1070 nm wavelength), operated at a spot size of 100 μm. The SLMed samples were produced in continuous laser mode: a scanning speed of 1000 mm/s with 250, 280 and 310 W laser powers, and 280 W laser power with 800, 1000 and 1200 mm/s, respectively. The hatch spacing was around 80 μm, the layer thickness was 25 μm, and the layers were scanned in a zigzag pattern, rotated by 67° between each successive layer to reduce the stress concentration.

2.2 Microstructural Characterization

The EBSD experiments were performed to obtain the grain size distribution, using an orientation imaging microscopy system attached to a JSM-6301 field emission microscope and

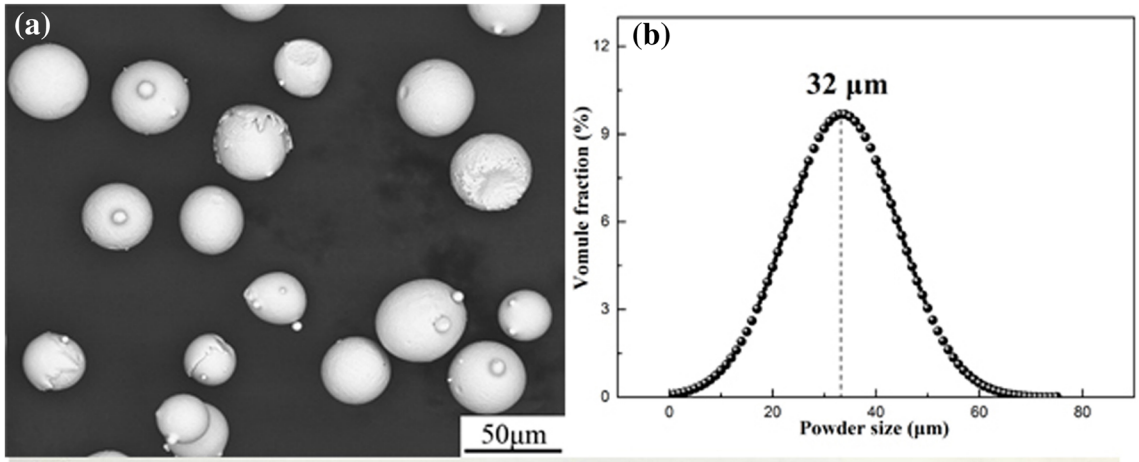

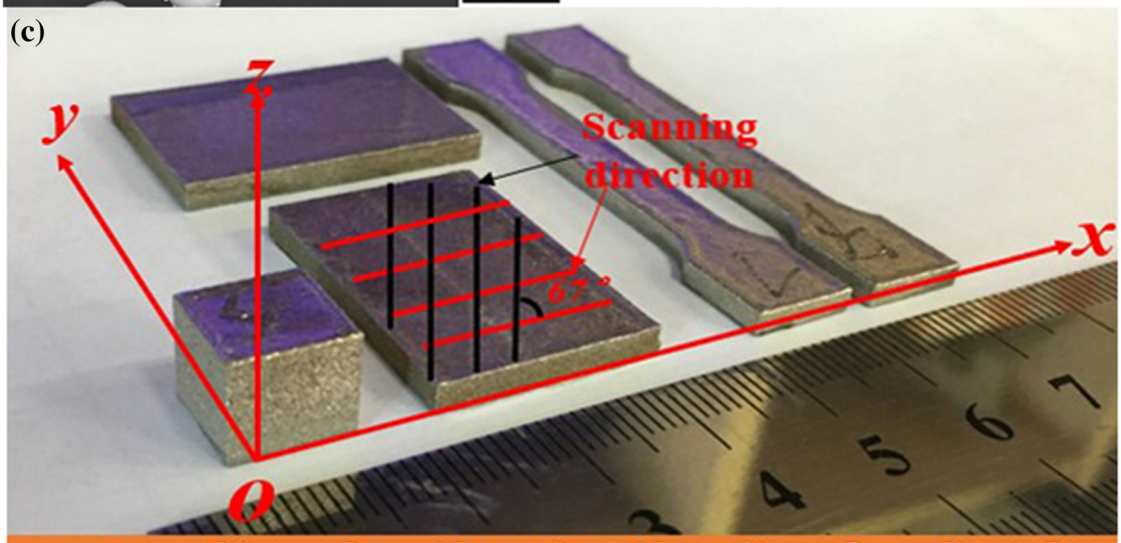

(wt. %)	Ni	Cr	Mo	C	Mn	Si	P	N	Fe
Wrought	balance	22.12	8.81	0.082	0.52	0.42	0.007	0.02	19.02
Powder	balance	21.45	8.73	0.075	0.45	0.45	0.006	0.02	18.99

Fig. 1 (a) The morphology of the powder particles, (b) the size distribution of the argon gas-atomized powder and (c) an image of the SLMed samples, including the scanning direction and the chemical compositions

the scanning step was 1 μm. The samples for EBSD experiments were first mechanically polished and then electro-polished in a solution of perchloric acid/ethanol = 1:9 (volume ratio) at a DC voltage of 13 V for 30 s. A FEI Tecnai G2 F20 transmission electron microscopy was used to compare the microstructures of the wrought and SLMed Hastelloy X.

2.3 Tensile Experiments

The tensile specimens were prepared based on the ASTM E8 procedure: 2 mm in thickness, with a gauge length of 25 mm and a gauge width of 6 mm. Specimens for tensile tests were ground with sequentially finer emery paper down to 2000# grit, where the grinding direction was parallel to the loading direction. The uniaxial tensile tests were conducted on a SANS power test machine at room temperature with a strain rate of 10^{-3} mm/s. The tensile direction was normal to the building direction, and three samples were repeated for each condition. The fracture surfaces were observed by SEM.

3. Results and Discussion

3.1 Microstructural Characterization

The grain sizes of the traditional wrought and SLMed Hastelloy X alloys were compared using EBSD, as shown in Fig. 2. It can be seen from the inverse pole figures that the Hastelloy X made by SLM was all austenite phase, and the wrought components had more regular polygonal grains than that of the samples fabricated by SLM. The grain boundaries were zigzag, and no twins were observed in the SLMed Hastelloy X alloy. There were more twin boundaries in wrought substrates with a 60° grain boundary angle, whereas there were more low-angle boundaries in the SLMed specimens as shown in Fig. 3. Usually, the more low-angle grain boundaries contribute the higher the yield strength.

In order to compare the microstructure, bright-field TEM images are observed for the wrought and SLMed Hastelloy X alloys in Fig. 4. Inside the grains, lines of dislocations were observed for the wrought sample as shown in Fig. 4(b), whereas many sub-grains were observed for the SLMed samples as shown in Fig. 4(d), and the dislocations were also present at the sub-grain boundaries of the as-received SLMed Hastelloy X alloys, which formed a significant dislocation-rich area and thus can retard or block the migration of newly formed dislocations under external force, resulting into a high strength (Ref 20, 25). Similar phenomenon was consistent with the results of other studies (Ref 25, 35). The metastable cellular structures were formed due to the combined effects of the Benard–Marangoni-driven instability and particle-accumulated structure formation during the SLM solidification process (Ref 36). Meanwhile, there were nano-inclusions distributed in the SLMed Hastelloy X alloy at the sub-grain boundaries as shown in Fig. 4(e). The size of the nano-inclusions was around 80 nm, which was much smaller than in the wrought substrate (1 μm), and they all revealed a remarkable enrichment in Mo, C and Si compared to the matrix, shown in Fig. 4(c) and (f), confirming the formation of Mo-rich carbides (Ref 37). In our SLMed Hastelloy X substrate, big inclusion was not found due to rapid solidification rates (typically range from 10^3-10^8 K/s), where there was 0.1-10 s for the nucleation and diffusional growth of precipitates in the wrought counterpart considering an approximate solidification rate of 273-373 K/s in traditional casting (Ref 28, 38, 39).

To compare and investigate the printing parameters on the mechanical properties of the wrought and SLMed Hastelloy X alloys, tensile experiments were conducted, and the results are given in Fig. 5. The ultimate tensile strength (UTS) values of the SLMed alloys were around 910 MPa and much higher than the wrought (∼ 750 MPa), as well as the yield strength (YS). The hardened structure for the SLMed

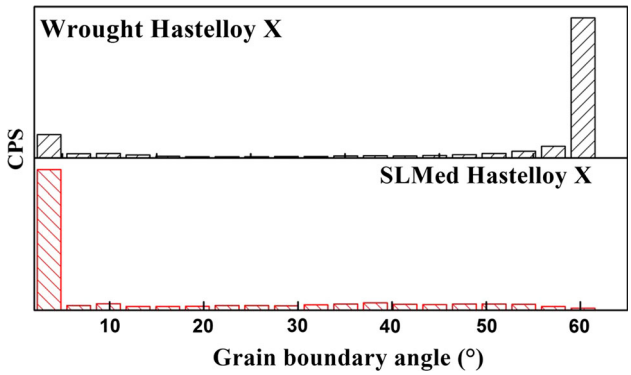

Fig. 3 Grain boundary angle distribution of the Hastelloy X alloys: (a) wrought and (b) SLMed

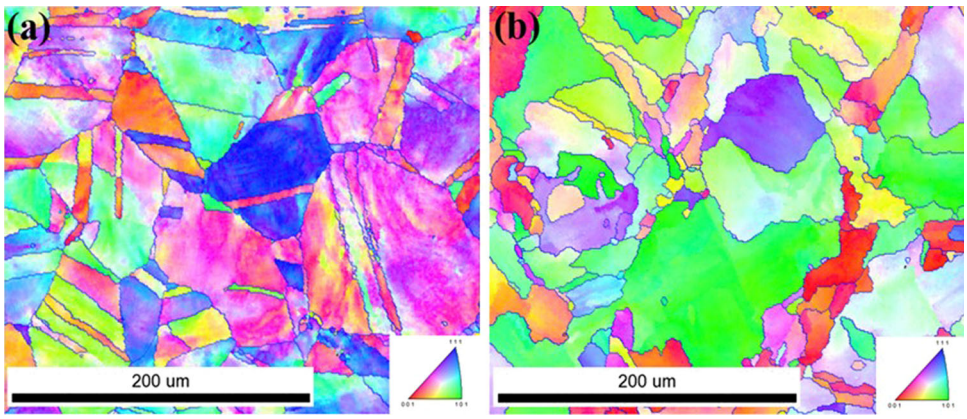

Fig. 2 Inverse pole figures of the Hastelloy X alloys: (a) wrought, (b) SLMed

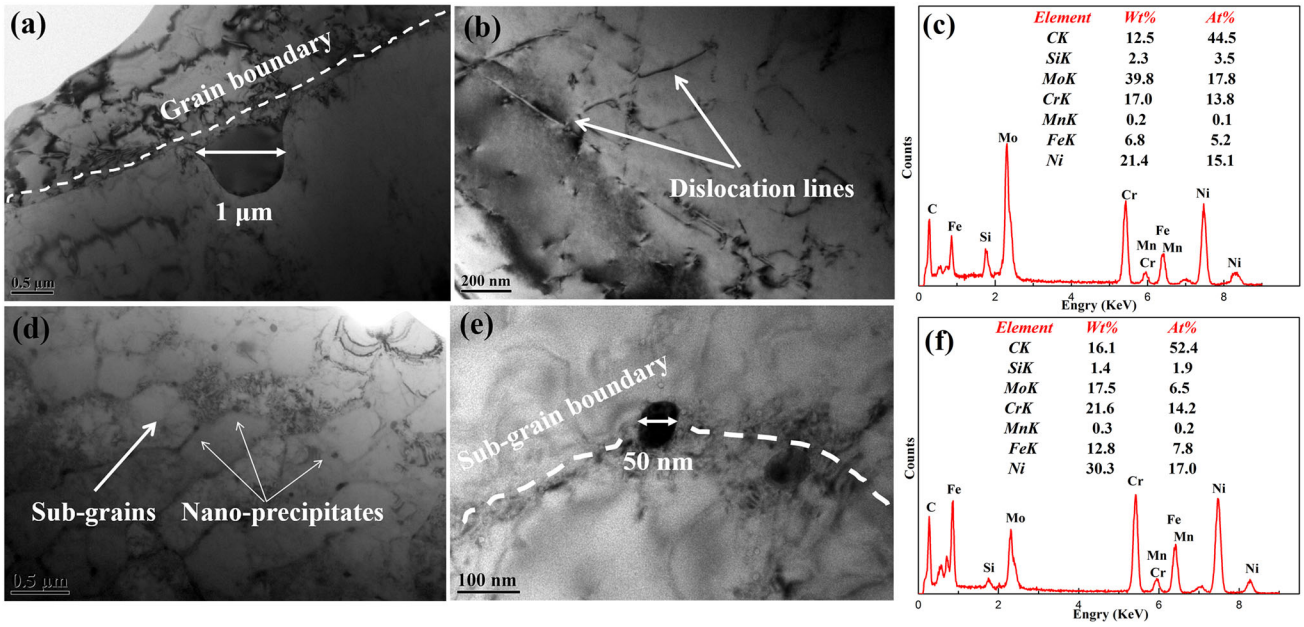

Fig. 4 Transmission electron microscopy images (bright field) and the EDS results of the Hastelloy X alloys: (a-c) wrought, (d-f) SLMed

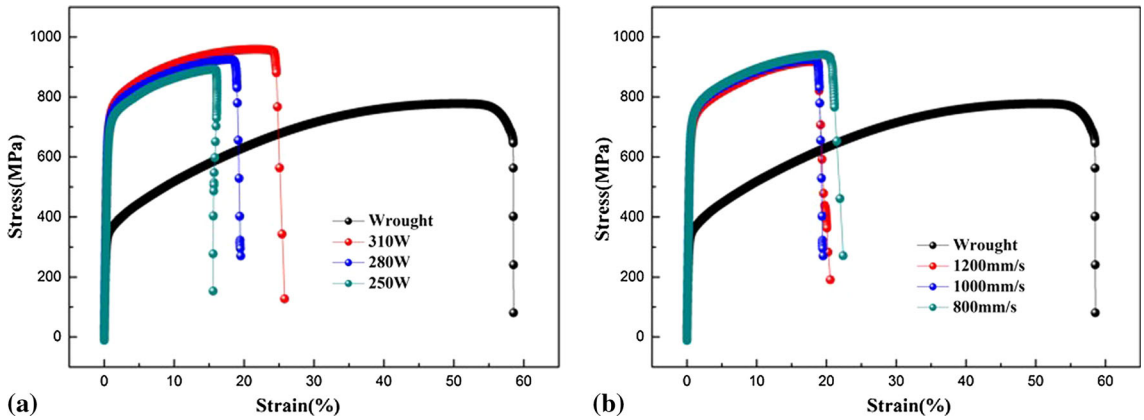

Fig. 5 Engineering stress vs. strain responses of the wrought and the SLMed Hastelloy X alloys

Hastelloy X alloys was mainly ascribed to the high-density dislocation. However, the percentage elongation after fracture for the SLMed Hastelloy X alloys (13-20%) was considerably smaller than that for the wrought counterpart (41%), and this should be mainly attributed to the pores existed in the SLMed matrix. Meanwhile, the molten pool boundaries also accelerate the fracture due to the poor binding force, and Wen et al. (Ref 40) pointed out these types of boundaries that can act as crack initiation sites under load conditions, that's why the elongation for the SLMed parts was much smaller than that of wrought (~ 41%). The different ductility can be also dropped out from the angle of the fracture and the tensile curve dropped sharply (a nearly 90° curve) when fracture of the SLMed Hastelloy X alloys occurred, while the wrought sample showed a necking transition before complete fracture. We can also see that the UTS and the elongation all increased with the increasing laser power and the decreasing scanning speed.

Since the pores have great effects on the mechanical properties of the SLMed parts, the porosities of the samples were evaluated by the Archimedes principle. The relative density of the SLMed Hastelloy X alloy at various laser energy densities is shown in Fig. 6, and the volumetric energy density (E_v) is calculated via Eq 1, which described the average energy per volume of powders (Ref 41, 42):

$$E_v = \frac{e}{rdt} \quad \text{(Eq 1)}$$

where e is the value of laser energy, r is the scanning rate, d is the hatch distance, and t is the thickness of powder layer. The process window for the highest relative density (approximately 99.0%) for the SLMed Hastelloy X alloy was in the range from 140 to 170 J/mm^3. In our work, the porosity decreased slightly with the increasing laser power or the decreasing scanning speed.

However, several authors doubted the availability of the volumetric energy density as an assessment criterion of the porosity, and they pointed out that some other printing parameters, such as hatch style and laser diameter, were disregarded, which can also affect the porosity (Ref 43).

Further investigations should be conducted systematically to clarify the relationship between the porosity and processing parameters.

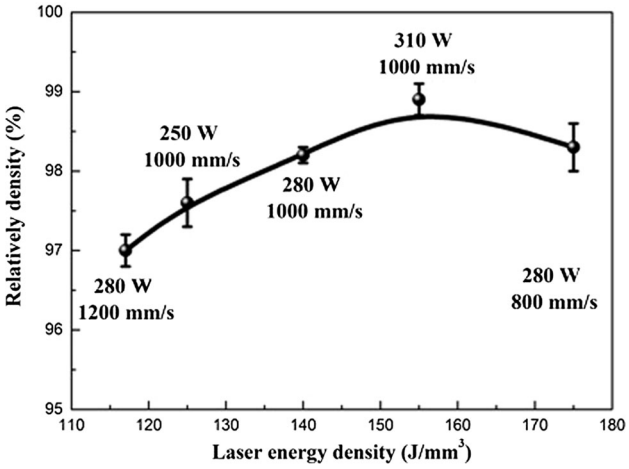

Fig. 6 Relative density of the SLMed Hastelloy X alloys at various laser energy densities

The macroscopic and microscopic morphologies of the Hastelloy X alloys after fracture are shown in Fig. 7, and typical dimple morphology for metallic fractures was widely observed for wrought Hastelloy X alloy, while many voids existed in the SLMed samples. Many small dimples were observed in the SLMed Hastelloy X alloy, related to the abundant sub-grain boundaries with a high concentration of dislocations and the premature instability, and fracture of the SLMed Hastelloy X alloy was largely attributed to the pores and molten pool boundaries near the surface. While there were many precipitates (Mo-rich carbides) on the fracture surface for the wrought Hastelloy X alloy as shown in Fig. 8(a) and (b), as a hard and brittle phase, those precipitates have a quite different deformation ratio from matrix, which would accelerate crack initiation. For the SLMed samples, there were many voids existed in the matrix, which lead to the poor elongation (Ref 23, 44, 45). The more the porosity is, the less of the ductility. In our work, the volumetric energy density for the best mechanical properties of the SLMed Hastelloy X alloy was therefore in the range from 140 to 170 J/mm^3. Meanwhile, pores also affect the durability of the SLMed parts, which is very necessary if additive techniques are to find widespread application (Ref 46-48). However, the size distribution of the pores on the SLMed

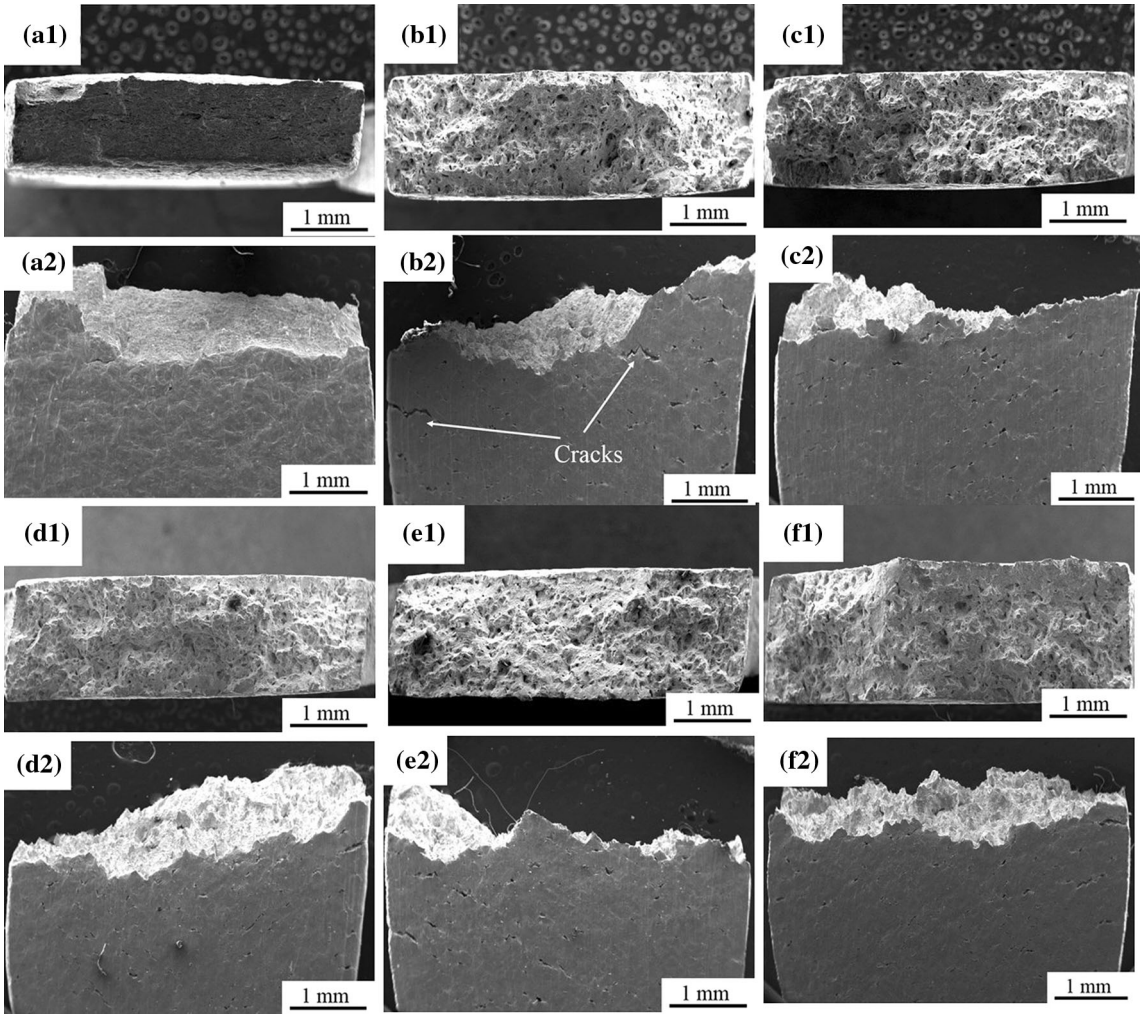

Fig. 7 Cross section and side view of the fractographic Hastelloy X alloys through SEM after tensile experiments: (a1, a2) wrought, (b1, b2) 250 W and 1000 mm/s, (c1, c2) 280 W and 1000 mm/s, (d1, d2) 310 W and 1000 mm/s, (e1, e2) 280 W and 800 mm/s, (f1, f2) 280 W and 1200 mm/s

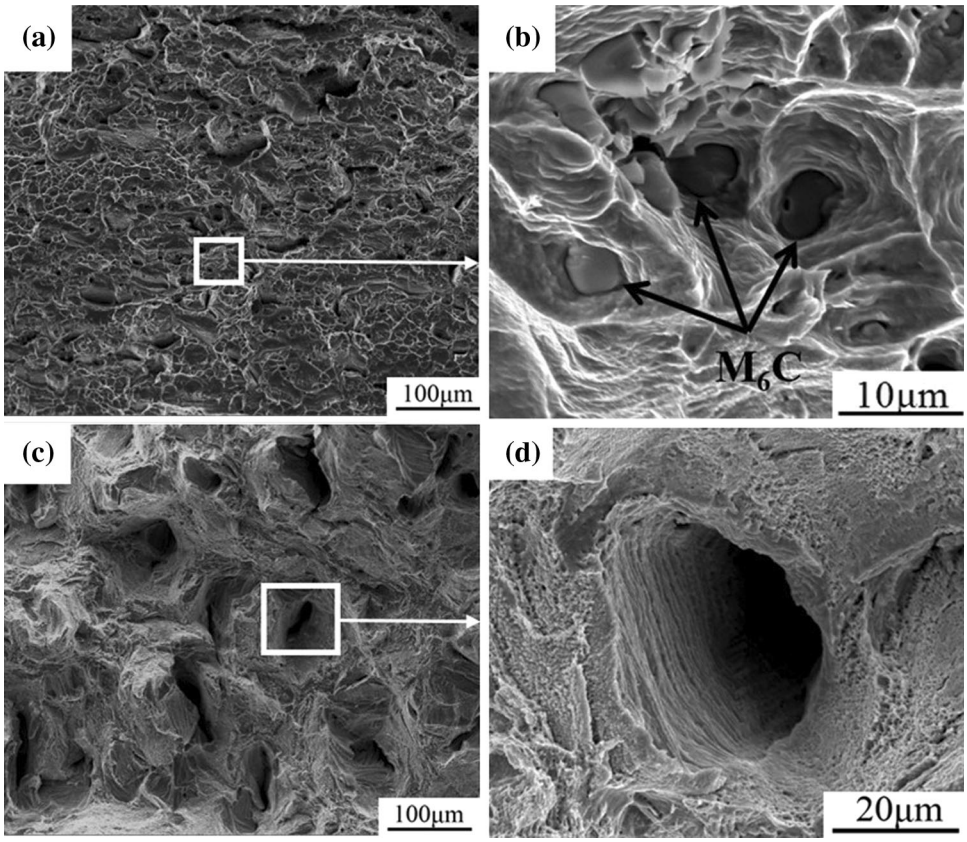

Fig. 8 Microscopic morphologies of the fractographic Hastelloy X alloys after tensile experiments: (a, b) wrought, (c, d) 280 W and 1000 mm/s

parts were not evaluated systematically in the existing literature, and further understanding of the effect of porosity, such as pore size and aspect ratio, on the mechanical properties of the SLMed parts needs to be clarified in further work.

4. Conclusions

In this work, the microstructure and mechanical properties of Hastelloy X alloy fabricated by SLM were investigated by EBSD, TEM, SEM and tensile experiments. The printing parameters, including laser power and laser scanning speed, on the mechanical properties of the SLMed Hastelloy X alloys were studied, and the results were compared with those of the wrought counterparts. The main conclusions were drawn as follows:

1. Nano-inclusions (Mo-rich carbides) distributed at the sub-grain boundaries in the SLMed Hastelloy X alloy due to the rapid solidification, whereas micron-scale precipitations existed in the wrought counterpart.
2. Molten pool boundaries widely existed in the SLMed matrix, which lead to poor plasticity. However, the UTS values of the SLMed Hastelloy X alloys were around 910 MPa and much higher than the wrought ($\sim$ 750 MPa), which was mainly ascribed to the high-density dislocation.
3. The UTS and the elongation for the SLMed samples all increased slightly with the increasing laser power and the decreasing scanning speed in our printing processes. The volumetric energy density for the best mechanical properties of the SLMed Hastelloy X alloy was in the range from 140 to 170 J/mm^3.

Acknowledgments

This work was supported by Shanghai Materials Genome Institute No. 5 (Project Number 16DZ2260605), Shanghai Sailing Program (Project Number 17YF1405400), Shanghai Research Institute of Materials Technology Innovation Project (18SG-07) and the project to strengthen industrial development at the grass-roots level (Project Number TC160A310/19).

References

1. H. Yin, J. Qiu, H. Liu, W. Liu, Y. Wang, Z. Fei, S. Zhao, X. An, J. Cheng, T. Chen, P. Zhang, G. Yu, and L. Xie, Effect of CrF 3 on the Corrosion Behaviour of Hastelloy-N and 316L Stainless Steel Alloys in FLiNaK Molten Salt, *Corros. Sci.*, 2018, **131**, p 355–364
2. C. Cabet and F. Rouillard, Corrosion of High Temperature Metallic Materials in VHTR, *J. Nucl. Mater.*, 2009, **392**(2), p 235–242
3. E.O. Olakanmi, R.F. Cochrane, and K.W. Dalgarno, A Review on Selective Laser Sintering/Melting (SLS/SLM) of Aluminium Alloy Powders: Processing, Microstructure, and Properties, *Prog. Mater. Sci.*, 2015, **74**, p 401–477
4. A.-N. Chen, J.-M. Wu, K. Liu, J.-Y. Chen, H. Xiao, P. Chen, C.-H. Li, and Y.-S. Shi, High-Performance Ceramic Parts with Complex Shape

Prepared by Selective Laser Sintering: A Review, *Adv. Appl. Ceram.*, 2017, **117**(2), p 100–117
5. D. Kong, X. Ni, C. Dong, X. Lei, L. Zhang, C. Man, J. Yao, X. Cheng, and X. Li, Bio-functional and Anti-corrosive 3D Printing 316L Stainless Steel Fabricated by Selective Laser Melting, *Mater Design*, 2018, **152**(5), p 88–101
6. D. Kong, X. Ni, C. Dong, L. Zhang, C. Man, J. Yao, K. Xiao, and X. Li, Heat Treatment Effect on the Microstructure and Corrosion Behavior of 316L Stainless Steel Fabricated by Selective Laser Melting for Proton Exchange Membrane Fuel Cells, *Electrochim. Acta*, 2018, **276**, p 293–303
7. K.M. Zhang, J.X. Zou, T. Grosdidier, C. Dong, and D.Z. Yang, Improved Pitting Corrosion Resistance of AISI, 316L Stainless Steel Treated by High Current Pulsed Electron Beam, *Surf. Coat. Technol.*, 2006, **201**(3-4), p 1393–1400
8. T.M. Yue, J.K. Yu, and H.C. Man, The Effect of Excimer Laser Surface Treatment on Pitting Corrosion Resistance of 316LS Stainless Steel, *Surf. Coat. Technol.*, 2001, **137**(1), p 65–71
9. D. Kong, C. Dong, X. Ni, and X. Li, Corrosion of Metallic Materials Fabricated by Selective Laser Melting, *NPJ Mater. Degrad.*, 2019, **3**, p 24
10. S. Van Bael, Y.C. Chai, S. Truscello, M. Moesen, G. Kerckhofs, H. Van Oosterwyck, I.P. Kruth, and J. Schrooten, The Effect of Pore Geometry on the In Vitro Biological Behavior of Human Periosteum-Derived Cells Seeded on Selective Laser-Melted Ti6Al4V Bone Scaffolds, *Acta Biomater.*, 2012, **8**(7), p 2824–2834
11. M.C. Karia, M.A. Popat, and K.B. Sangani, Selective Laser Melting of Inconel Super Alloy—A Review, *AIP Conf. Proc.*, 2017, **1859**, p 020013
12. J.L. Zhang, B. Song, Q.S. Wei, D. Bourell, and Y.S. Shi, A Review of Selective Laser Melting of Aluminum Alloys: Processing, Microstructure, Property and Developing Trends, *J. Mater. Sci. Technol.*, 2019, **35**(2), p 270–284
13. G. Miranda, S. Faria, F. Bartolomeu, E. Pinto, S. Madeira, A. Mateus, P. Carreira, N. Alves, F.S. Silva, and O. Carvalho, Predictive Models for Physical and Mechanical Properties of 316L Stainless Steel Produced by Selective Laser Melting, *Mater. Sci. Eng. A-Struct.*, 2016, **657**, p 43–56
14. M.S.F. de Lima and S. Sankare, Microstructure and Mechanical Behavior of Laser Additive Manufactured AISI, 316 Stainless Steel Stringers, *Mater Design*, 2014, **55**, p 526–532
15. J.A. Cherry, H.M. Davies, S. Mehmood, N.P. Lavery, S.G.R. Brown, and J. Sienz, Investigation into the Effect of Process Parameters on Microstructural and Physical Properties of 316L Stainless Steel Parts by Selective Laser Melting, *Int. J. Adv. Manuf. Technol.*, 2015, **76**(5–8), p 869–879
16. B.C. Zhang, L. Dembinski, and C. Coddet, The Study of the Laser Parameters and Environment Variables Effect on Mechanical Properties of High Compact Parts Elaborated by Selective Laser Melting 316L Powder, *Mater. Sci. Eng. A-Struct.*, 2013, **584**, p 21–31
17. F.X. Xie, X.B. He, S.L. Cao, and X.H. Qu, Structural and Mechanical Characteristics of Porous 316L Stainless Steel Fabricated by Indirect Selective Laser Sintering, *J. Mater. Process. Technol.*, 2013, **213**(6), p 838–843
18. R.D. Li, J.H. Liu, Y.S. Shi, M.Z. Du, and Z. Xie, 316L Stainless Steel with Gradient Porosity Fabricated by Selective Laser Melting, *J. Mater. Eng. Perform.*, 2010, **19**(5), p 666–671
19. N.J. Harrison, I. Todd, and K. Mumtaz, Reduction of Micro-cracking in Nickel Superalloys Processed by Selective Laser Melting: A Fundamental Alloy Design Approach, *Acta Mater.*, 2015, **94**, p 59–68
20. D. Kong, X. Ni, C. Dong, L. Zhang, C. Man, X. Cheng, and X. Li, Anisotropy in the Microstructure and Mechanical Property for the Bulk and Porous 316L Stainless Steel Fabricated Via Selective Laser Melting, *Mater. Lett.*, 2019, **235**, p 1–5
21. X. Ni, D. Kong, W. Wu, L. Zhang, C. Dong, B. He, L. Lu, K. Wu, and D. Zhu, Corrosion Behavior of 316L Stainless Steel Fabricated by Selective Laser Melting Under Different Scanning Speeds, *J. Mater. Eng. Perform.*, 2018, **27**, p 3667
22. J.J. Lewandowski and M. Seifi, Metal Additive Manufacturing: A Review of Mechanical Properties, *Annu. Rev. Mater. Res.*, 2016, **46**, p 151–186
23. Y. Kok, X.P. Tan, P. Wang, M.L.S. Nai, N.H. Loh, E. Liu, and S.B. Tor, Anisotropy and Heterogeneity of Microstructure and Mechanical Properties in Metal Additive Manufacturing: A Critical Review, *Mater Design*, 2018, **139**, p 565–586
24. D. Kong, C. Dong, X. Ni, L. Zhang, C. Man, J. Yao, Y. Ji, Y. Ying, K. Xiao, X. Cheng, and X. Li, High-Throughput Fabrication of Nickel-Based Alloys with Different Nb Contents Via A Dual-Feed Additive Manufacturing System: Effect of Nb Content on Microstructural and Mechanical Properties, *J. Alloys Compd.*, 2019, **785**, p 826–837
25. K. Saeidi, X. Gao, Y. Zhong, and Z.J. Shen, Hardened Austenite Steel with Columnar Sub-grain Structure Formed by Laser Melting, *Mater. Sci. Eng. A-Struct.*, 2015, **625**, p 221–229
26. R.D. Li, P.D. Niu, T.C. Yuan, P. Cao, C. Chen, and K.C. Zhou, Selective Laser Melting of an Equiatomic CoCrFeMnNi High-Entropy Alloy: Processability, Non-equilibrium Microstructure and Mechanical Property, *J. Alloys Compd.*, 2018, **746**, p 125–134
27. S.C. Luo, P. Gao, H.C. Yu, J.J. Yang, Z.M. Wang, and X.Y. Zeng, Selective Laser Melting of an Equiatomic AlCrCuFeNi High-Entropy Alloy: Processability, Non-equilibrium Microstructure and Mechanical Behavior, *J. Alloys Compd.*, 2019, **771**, p 387–397
28. C. Man, C. Dong, T. Liu, D. Kong, D. Wang, and X. Li, The Enhancement of Microstructure on the Passive and Pitting Behaviors of Selective Laser Melting 316L SS in Simulated Body Fluid, *Appl. Surf. Sci.*, 2019, **467–468**, p 193–205
29. C. Man, Z.W. Duan, Z.Y. Cui, C.F. Dong, D.C. Kong, T.T. Liu, S.G. Chen, and X. Wang, The Effect of Sub-grain Structure on Intergranular Corrosion of 316L Stainless Steel Fabricated Via Selective Laser Melting, *Mater. Lett.*, 2019, **243**, p 157–160
30. T. Trosch, J. Strossner, R. Yolkl, and U. Glatzel, Microstructure and Mechanical Properties of Selective Laser Melted Inconel 718 Compared to Forging and Casting, *Mater. Lett.*, 2016, **164**, p 428–431
31. A. Rottger, K. Geenen, M. Windmann, F. Binner, and W. Theisen, Comparison of Microstructure and Mechanical Properties of 316 L Austenitic Steel Processed by Selective Laser Melting with Hot-Isostatic Pressed and Cast Material, *Mater. Sci. Eng. A-Struct.*, 2016, **678**, p 365–376
32. J. Suryawanshi, K.G. Prashanth, and U. Ramamurty, Mechanical Behavior of Selective Laser Melted 316L Stainless Steel, *Mater. Sci. Eng. A-Struct.*, 2017, **696**, p 113–121
33. J.H. Martin, B.D. Yahata, J.M. Hundley, J.A. Mayer, T.A. Schaedler, and T.M. Pollock, 3D Printing of High-Strength Aluminium Alloys, *Nature*, 2017, **549**(7672), p 365
34. D. Tomus, P.A. Rometsch, M. Heilmaier, and X. Wu, Effect of Minor Alloying Elements on Crack-Formation Characteristics of Hastelloy-X Manufactured by Selective Laser Melting, *Addit. Manuf.*, 2017, **16**, p 65–72
35. D. Kong, C. Dong, X. Ni, L. Zhang, J. Yao, C. Man, X. Cheng, K. Xiao, and X. Li, Mechanical Properties and Corrosion Behavior of Selective Laser Melted 316L Stainless Steel After Different Heat Treatment Processes, *J. Mater. Sci. Technol.*, 2019, **35**, p 1499
36. K.G. Prashanth and J. Eckert, Formation of Metastable Cellular Microstructures in Selective Laser Melted Alloys, *J. Alloys Compd.*, 2017, **707**, p 27–34
37. X.Y. Wang, K. Kurosawa, M. Huang, X.K. Lu, D. Zhang, H. Kokawa, Y.B. Yan, and S. Yang, Control of Precipitation Behaviour of Hastelloy-X Through Grain Boundary Engineering, *Mater. Sci. Technol. Lond.*, 2017, **33**(17), p 2078–2085
38. M. Suzuki, K. Murakami et al., Inclusion Particle Growth During Solidification of Stainless Steel, *Trans. Iron Steel Inst. Jpn.*, 2007, **41**(3), p 247–256
39. X.-Q. Ni, D.-C. Kong, Y. Wen, L. Zhang, W.-H. Wu, B.-B. He, L. Lu, and D.-X. Zhu, Anisotropy in Mechanical Properties and Corrosion Resistance of 316L Stainless Steel Fabricated by Selective Laser Melting, *Int. J. Min. Metall. Mater.*, 2019, **26**(3), p 319–328
40. S.F. Wen, S. Li, Q.S. Wei, C.Z. Yan, Z. Sheng, and Y.S. Shi, Effect of Molten Pool Boundaries on the Mechanical Properties of Selective Laser Melting Parts, *J. Mater. Process. Technol.*, 2014, **214**(11), p 2660–2667
41. S.M. Yusuf and N. Gao, Influence of Energy Density on Metallurgy and Properties in Metal Additive Manufacturing, *Mater. Sci. Technol. Lond.*, 2017, **33**(11), p 1269–1289
42. J. Kluczynski, L. Sniezek, K. Grzelak, and J. Mierzynski, The Influence of Exposure Energy Density on Porosity and Microhardness of the SLM Additive Manufactured Elements, *Materials*, 2018, **11**(11), p E2304

43. K.G. Prashanth, S. Scudino, T. Maity, J. Das, and J. Eckert, Is the Energy Density a Reliable Parameter for Materials Synthesis by Selective Laser Melting?, *Mater. Res. Lett.*, 2017, **5**(6), p 386–390
44. W.E. Frazier, Metal Additive Manufacturing: A Review, *J. Mater. Eng. Perform.*, 2014, **23**(6), p 1917–1928
45. D.W. Rosen, A Review of Synthesis Methods for Additive Manufacturing, *Virtual Phys. Prototyp.*, 2016, **11**(4), p 305–317
46. H. Zhang, D. Gu, L. Xi, H. Zhang, M. Xia, and C. Ma, Anisotropic Corrosion Resistance of TiC Reinforced Ni-Based Composites Fabricated by Selective Laser melting, *J. Mater. Sci. Technol.*, 2019, **35**(6), p 1128–1136
47. D.C. Kong, A.N. Xu, C.F. Dong, F.X. Mao, K. Xiao, X.G. Li, and D.D. Macdonald, Electrochemical Investigation and Ab Initio Computation of Passive Film Properties on Copper in Anaerobic Sulphide Solutions, *Corros. Sci.*, 2017, **116**, p 34–43
48. D.C. Kong, C.F. Dong, X.Q. Ni, A.N. Xu, C. He, K. Xiao, and X.G. Li, Long-Term Polarisation and Immersion for Copper Corrosion in High-Level Nuclear Waste Environment, *Mater. Corros.*, 2017, **68**(10), p 1070–1079